Geochronology, 6, 621–638, 2024
https://doi.org/10.5194/gchron-6-621-2024


# µID-TIMS: spatially resolved high-precision U–Pb zircon geochronology

**Sava Markovic[1], Jörn-Frederik Wotzlaw[1], Dawid Szymanowski[1], Joakim Reuteler[2], Peng Zeng[2], and Cyril Chelle-Michou[1]**

[1]Institute of Geochemistry and Petrology, ETH Zurich, 8092 Zurich, Switzerland
[2]Scientific Center for Optical and Electron Microscopy (ScopeM) ETH Zurich, 8093 Zurich, Switzerland

**Correspondence:** Sava Markovic (sava.markovic@eaps.ethz.ch)

Received: 17 June 2024 – Discussion started: 2 July 2024
Revised: 9 September 2024 – Accepted: 29 September 2024 – Published: 26 November 2024

**Abstract.** We present a novel methodology for spatially resolved high-precision U–Pb geochronology of individual growth domains in complex zircon. Our approach utilizes a multi-ion-species ($Xe^+/Ar^+$) plasma focused ion beam (PFIB)–femtosecond (fs) laser system equipped with a scanning electron microscope (SEM). This system enables micrometer-resolution sampling of zircon growth domains with real-time monitoring by cathodoluminescence SEM imaging. Microsamples are then extracted, chemically abraded, dissolved, and analyzed by isotope dilution thermal ionization mass spectrometry (ID-TIMS) to obtain high-precision U–Pb dates. For its superior beam precision (∼ 8–20 µm diameter), cleaner cuts, and negligible nanometer-scale damage imparted on the zircon structure, PFIB machining (30 kV) is preferred for microsamples of sizes expected in most future studies focusing on texturally complex natural zircon (20–120 µm length scales). Femtosecond laser machining is significantly faster and therefore more appropriate for larger microsamples (>120 µm length scales), but it is also coarser (≥ 20 µm probe size), produces rougher cuts, and creates a micrometer-scale-wide structurally damaged zone along the laser cuts (i.e., 2 orders of magnitude wider compared to PFIB). Our experiments show that PFIB machining can be conducted on zircon coated with carbon and protective metal coatings as neither offset the U–Pb systematics, nor do they introduce trace amounts of common Pb. We used a $Xe^+$ PFIB and femtosecond laser to obtain U–Pb dates for Mud Tank and GZ7 zircon microsamples covering a range of sizes (40 × 18 × 40–100 × 80 × 70 µm) and found that microsampling does not bias the accuracy of the resulting µID-TIMS U–Pb dates. The accuracy and precision of µID-TIMS dates for zircon of any given age depend, as for non-microsampled zircon, on the available mass of U and radiogenic Pb – both a function of sample size. Our accompanying open-source code can aid researchers in estimating the necessary microsample size needed to obtain accurate dates at precision sufficient to resolve the processes under study. µID-TIMS bridges the gap between conventional bulk-grain high-precision dating and high-spatial-resolution in situ techniques, enabling the study of the timescales of a variety of processes recorded on the scale of individual growth zones in zircon. This method can be applied to zircon of any age and composition, from terrestrial systems to precious samples from other planetary bodies.

## 1 Introduction

High-precision U–Pb zircon geochronology has revolutionized the Earth sciences by providing a numerical calibration to the geological timescale and quantifying ages and rates of processes from planetary differentiation to impacts, supereruptions, and mass extinctions (Bowring et al., 1998; Bowring and Schmitz, 2003; Schaltegger et al., 2008; Blackburn et al., 2013; Iizuka et al., 2015; Schoene et al., 2015; Wotzlaw et al., 2015; Davies et al., 2017; Schoene et al., 2019). The method relies on accurate and precise measurements of isotope ratios of two parent–daughter systems of uranium and lead ($^{238}U/^{206}Pb$ and $^{235}U/^{207}Pb$), the proportion of which is a function of time elapsed since a zircon crystallized. Several features of the zircon U–Pb system have established it as the most reliable and widely ap-

plied geochronometer: (1) zircon is robust under a range of geological conditions, (2) two independent U–Pb decay systems enable testing of closed-system behavior, (3) negligible amounts of non-radiogenic (i.e., common) Pb are incorporated in zircon during crystallization, and (4) zircon is widespread in crustal rocks.

Zircon growth zones record ambient conditions in host magmas during continuous crystal growth or punctuated crystallization episodes thousands to millions of years apart (e.g., Corfu et al., 2003; Hawkesworth et al., 2004; Costa et al., 2008; Wotzlaw et al., 2012; Samperton et al., 2015; Chelle-Michou et al., 2017; Szymanowski et al., 2017, 2023; Farina et al., 2018; Costa et al., 2020; Curry et al., 2021; Tavazzani et al., 2023). However, quantifying rates of processes recorded as textural and compositional complexities in individual zircon crystals is challenging with current analytical techniques applied to U–Pb geochronology. Isotope dilution thermal ionization mass spectrometry (ID-TIMS), where whole grains or crystal fragments are dissolved for analysis, grants the required analytical precision but largely neglects intra-grain age complexities, collapsing the entire zircon growth history into a precise, volume-averaged date (Schoene, 2014; Schaltegger et al., 2015a; Schoene and Baxter, 2017). On the other hand, in situ dating with laser ablation inductively coupled plasma mass spectrometry (LA-ICP-MS) or secondary ion mass spectrometry (SIMS) enables targeting of individual growth zones (10–50 µm beam size) but usually at insufficient precision to resolve intra-grain age differences at $10^3$–$10^4$-year resolution. An analytical protocol that would combine the best of both worlds to accurately resolve intra-grain age differences in complex zircon at an age resolution better than the timescales of the investigated processes has thus been a long-envisaged but as yet unattained goal of the U–Pb geochronological community.

Physical sampling of crystal domains within individual zircon for high-precision dating has long been conceived as a way to overcome the respective limitations of in situ and bulk-grain dating. To this end, researchers have been cutting zircons with a wire saw ("microtome"; Sergeev et al., 1997; Sergeev and Steiger, 1998) and breaking them with a scalpel (e.g., Barboni et al., 2015; Samperton et al., 2015), although such mechanical techniques offered limited control regarding the requirement of textural homogeneity of isolated fragments. Nanosecond laser sectioning (15–20 µm spatial resolution) on double-polished zircon (∼ 30 µm thick wafers) previously imaged for internal zoning has also been explored; however, the effects of using the nanosecond laser and associated damage on U–Pb systematics have not yet been documented (Crowley, 2018; Kovacs et al., 2020; Rioux et al., 2023). More recently, White et al. (2020) introduced a focused ion beam sampling technique in a petrographic context for U–Pb dating of baddeleyite crystals, which shows great potential to be adapted for microsampling of zircon.

In pursuit of dating individual growth domains in complex zircon at high precision, we present a methodology that we call µID-TIMS. Our method utilizes a coupled plasma focused ion beam (PFIB)–femtosecond laser machining system for texturally controlled zircon microsampling in preparation for high-precision dating by chemical abrasion (CA-)ID-TIMS. We first discuss the overall performance and applicability of PFIB and femtosecond laser machining for zircon microsampling. Then, we evaluate the impact of the microsampling procedure (coating and structural damage) on U–Pb zircon systematics. We then present U–Pb isotope results for a number of PFIB- and femtosecond-laser-machined microsamples of the Mud Tank (∼ 700–730 Ma) and GZ7 (∼ 530 Ma) zircon reference materials to discuss the accuracy and precision of U–Pb dates obtained with our method. Finally, we present a code for assessing the feasibility of a zircon microsampling study in terms of accuracy and precision, and we discuss future research applications of µID-TIMS.

## 2 Rationale for using a plasma focused ion beam (PFIB) and femtosecond laser for zircon microsampling

An adequate machining tool for zircon microsampling should ideally satisfy three criteria: (1) it should have fine enough machining precision (i.e., beam size and sharpness) to ensure microsampling of homogeneous growth zones; (2) microsampling should be manageable within workable times, as these are a priority for conducting a cost- and time-effective study; and (3) machining should introduce no bias in the U–Pb systematics of analyzed microsamples.

Figure 1 compares the resolution and speed of different machining techniques. Zircon microsampling requires precision from a few micrometers, for the finest cuts, to tens or hundreds of micrometers for faster machining of larger volumes. Gas field ionization source (GFIS) and liquid metal ion source (LMIS) FIB are likely too fine and too slow for the purpose. A plasma focused ion beam (PFIB) employing different ion species ($Xe^+$, $Ar^+$, $N^+$, $O^+$) covers the range of machining precision required for zircon microsampling from micrometers to tens of micrometers by varying the ion beam current (1 pA to 4 µA), and we found that $Ar^+$ and $Xe^+$ perform best on zircon in terms of milling speed and cut quality. The 515 nm wavelength femtosecond laser has a somewhat larger beam size (>20 µm) compared to PFIB operated at the highest currents but achieves an order of magnitude faster milling (>10 000 $\mu m^3\ min^{-1}$ compared to <1000 $\mu m^3\ min^{-1}$; Fig. 1). Thus, of the currently available micromachining techniques, we identify PFIB and the femtosecond laser as tools with high potential for application to zircon microsampling. Both methods are explored below, focusing in particular on associated structural damage, effects of coating, and the quality of the obtained U–Pb data.

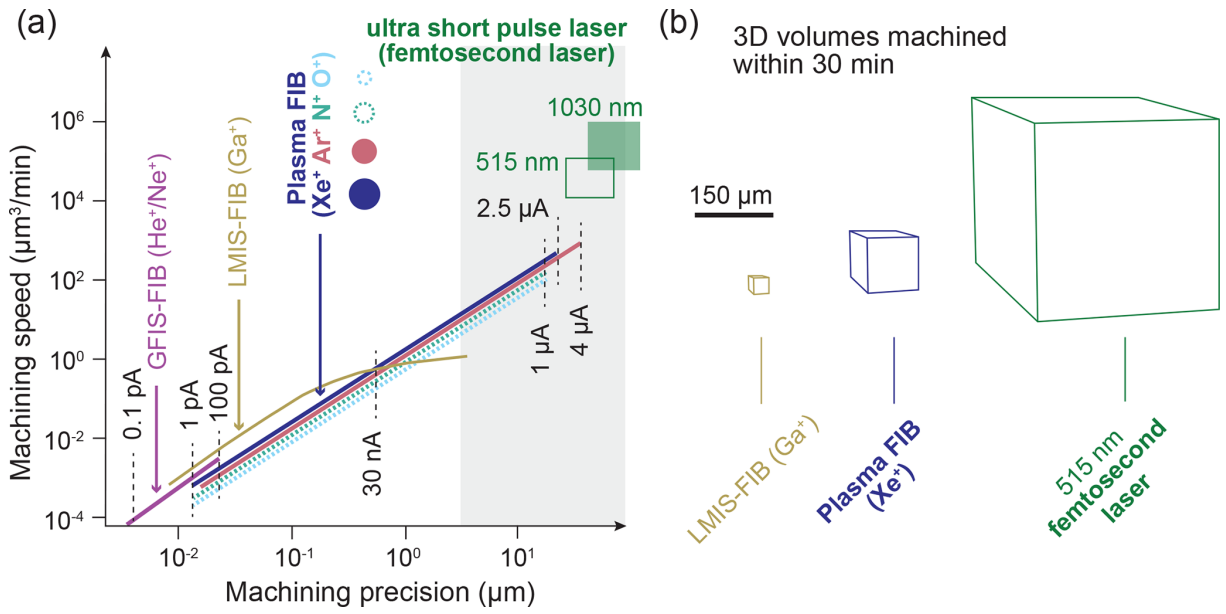


**Figure 1.** **(a)** Precision versus speed of different machining techniques (e.g., Echlin et al., 2015; Smith et al., 2014). Precision (beam size) is shown as a function of ion species for the FIB and different wavelengths (515 and 1030 nm) for the femtosecond laser. **(b)** Volume of Si machinable within 30 min with the $Ga^+$ FIB (100 nA ion beam current) and $Xe^+$ PFIB (~2 µA), as well as the femtosecond laser operated at 515 nm wavelength. FIB – focused ion beam, GFIS – gas field ionization source, LMIS – liquid metal ion source.

## 3 Materials and experimental protocol

### 3.1 Textural and chemical characterization of zircon

Test samples used in this study include megacrysts of the natural zircon reference materials Mud Tank (700–730 Ma and 9 ppm U; Woodhead and Hergt, 2005; Horstwood et al., 2016; Gain et al., 2019) and GZ7 (530 Ma and 650 ppm U; Nasdala et al., 2018), as well as zircon crystals from the Lava Creek Tuff (LCT-A; Wotzlaw et al., 2015) and the Owens Gully Diorite (OG-1; Stern et al., 2009; Kemp et al., 2017). All zircon crystals were first thermally annealed at 900 °C for 48 h, embedded in 1 in. epoxy mounts, and ground and polished to expose crystal interiors. Cathodoluminescence (CL) imaging of the internal texture of zircon was carried out on a JEOL JSM-6390 LA scanning electron microscope (SEM) equipped with a Deben Centaurus CL detector or on a Quanta 200F FEG-SEM with a Gatan MiniCL system. In situ trace element composition and U–Pb isotope systematics of the test crystals were analyzed with a S155-LR ASI Resolution 193 nm excimer laser ablation (LA) system coupled to a Thermo Scientific Element-XR sector-field inductively coupled plasma mass spectrometer (see Supplement Fig. S1 and Table S1). Trace element and U–Pb isotope signals were collected simultaneously by employing a laser spot size of 29 µm, a repetition rate of 5 Hz, and an energy density of 2 J $cm^{-2}$. GJ-1 zircon and NIST 610 glass were used as primary reference materials for U–Pb dating and quantifying element concentrations, respectively, whereas zircons 91500, AUSZ7-1, AUSZ7-5, Plešovice, and Temora served as secondary reference materials (Wiedenbeck et al., 1995, 2004; Black et al., 2004; Jackson et al., 2004; Slama et al., 2008; Kennedy et al., 2014; von Quadt et al., 2016). Raw output data were processed using Iolite 4 (Paton et al., 2011).

### 3.2 Plasma focused ion beam (PFIB) and femtosecond laser zircon micromachining

Zircon microsamples were machined on a Helios 5 Laser Hydra UX system (Thermo Fisher Scientific), whereas ion irradiation experiments (Sect. 3.3) were additionally carried out on a Fera3 $Xe^+$ PFIB system (Tescan; ScopeM, ETH Zurich). The Helios 5 system integrates multi-ion-species plasma FIB ($Xe^+$, $Ar^+$, $O^+$, $N^+$), a femtosecond laser, and an SEM equipped with a CL detector into one device (Fig. 2). The three columns are fixed in space, and zircon machining from different angles is achieved through sample rotation (0–360°) and tilt (−10–57° for standard 1 in. mounts and −38–60° for 0.5 in. mounts and laser objective removed) from the coincidence point of the three columns or using a pre-tilted sample holder for normal-incidence femtosecond laser machining (Fig. 2). Machining and process monitoring are achieved by alternating between femtosecond laser or PFIB micromachining steps that are seconds to minutes long and electron imaging on the (CL-)SEM. PFIB machining was done on zircon embedded in epoxy, polished and coated with a 20 nm layer of carbon.

PFIB machining (Figs. S2 and S3) involved initial bulk trenching in the front, back, and side of the incipient microsample with a normal-incident-angle ion beam operated

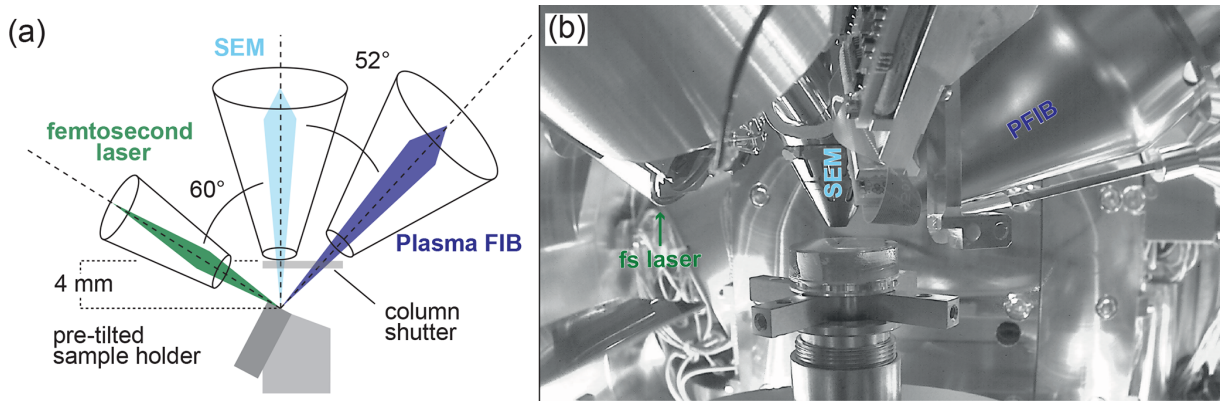


**Figure 2.** **(a)** Geometry of the Helios 5 Hydra PFIB–femtosecond laser–scanning electron microscope system equipped with a cathodoluminescence detector. **(b)** Sample chamber view showing the main elements. SEM – scanning electron microscope.

at the highest current (2.5 µA). Removing enough material in these initial steps is important to provide open space laterally to achieve enough depth (i.e., avoid material redeposition) in the following steps. Back and front trenches were then progressively deepened and microsamples shaped into a trapezoid geometry with a lower-current (1 µA) ion beam at a $45 \pm 4°$ incident angle (3 to 11°stage tilt). The microsamples were finally undercut and left attached to the rest of the zircon only via a narrow side bridge (0.5–1 µA at ∼45° beam incident angle). Zircon machining was performed at a 30 kV ion beam voltage. The machining depth was controlled by applying an ion dose (in µm, calibrated to silicon milling) 3 times the desired depth (empirical relationship for zircon milling).

Femtosecond laser machining was performed at a 60° angle with respect to the mount surface (i.e., no use of the pre-tilted holder) employing a 515 nm laser wavelength (Fig. S4). The microsamples were isolated from the surrounding zircon by successive machining and 90° rotation to achieve enough depth before undercutting. At each step, the femtosecond laser was operated at a 6 kHz pulse frequency, 0.048 W power, and pulse energy of 8 µJ, employing vertical and horizontal polarization.

### 3.3 Transmission electron microscopy of PFIB- and femtosecond-laser-irradiated zircon

Structural damage (amorphization, creation of point defects, and ion implantation) induced during PFIB and femtosecond laser microsampling was analyzed on a high-resolution (∼0.16 nm) Talos F200X transmission electron microscope (TEM) at ScopeM, ETH Zurich. For this purpose, electron transparent (≤100 nm thin) lamellae oriented perpendicular to the ion- and laser-irradiated surfaces, and one additional lamella from a microsample wall, were prepared using a Helios 5UX $Ga^+$ FIB. $Ga^+$ was the preferred ion species for isolating the effects of previous $Xe^+/Ar^+$ irradiation with high precision. The TEM images were acquired with a 200 kV electron beam voltage in both standard TEM and scanning (STEM) mode. Besides structural analysis, element distribution maps of TEM lamellae were acquired using a Super-X energy-dispersive X-ray spectrometer (EDS) on the Talos TEM.

### 3.4 High-precision (CA-ID-TIMS) U–Pb zircon geochronology

For CA-ID-TIMS, zircon microsamples were detached from the bulk zircon with a scalpel by breaking the bridge. Zircons were washed in 6 N HCl and $HNO_3$ to remove surface impurities, then loaded into 200 µL perfluoroalkoxy (PFA) microcapsules in one drop of $HNO_3$ and chemically abraded (CA) in ∼50 µL of added 29 M HF at 190–210 °C between 10–14 h to selectively dissolve domains affected by radiation damage. Following CA, zircon aliquots were washed in 6 N HCl on a hotplate and in 3.5 N $HNO_3$ in an ultrasonic bath. After washing, the zircons were loaded back into their respective microcapsules, spiked with one drop (3–11 mg) of ($^{202}$Pb–)$^{205}$Pb–$^{233}$U–$^{235}$U ET(2)535 tracer solution (Condon et al., 2015; McLean et al., 2015), and dissolved over 60 h in ∼70 µm of 29 M HF at 210 °C in a Parr bomb. After dissolution, the samples were dried down and re-dissolved in 6 N HCl at 180 °C for several hours, dried down, and then re-dissolved again in 3 N HCl. Uranium and lead were separated from matrix elements using an HCl-based single-column ion-exchange chromatography procedure modified from Krogh (1973) and dried down with one drop of 0.02 M $H_3PO_4$. The samples were re-dissolved in a ∼1–2 µL drop of Si-gel emitter (Gerstenberger and Haase, 1997) and loaded onto outgassed zone-refined Re filaments.

Isotope ratios of $UO_2$ and Pb were analyzed on a Thermo Triton Plus TIMS instrument in static mode with Faraday cups connected to $10^{13}\,\Omega$ amplifiers or alternatively by peak hopping on a MasCom secondary electron multiplier (von Quadt et al., 2016; Wotzlaw et al., 2017). Data reduction, date calculation, and uncertainty propagation were carried

out using the Tripoli and ET_Redux software (Bowring et al., 2011) with algorithms of McLean et al. (2011). U–Pb isotope ratios and corresponding dates were calculated relative to the published calibration of the ET tracer solutions (Condon et al., 2015) using the decay constants of Jaffey et al. (1971) and assuming U-blank mass of $0.32 \pm 0.08$ pg (1 SD; see Fig. S14b and Sect. 4.3.2) and $^{238}U/^{235}U$ of the sample and blank of $137.818 \pm 0.045$ (Hiess et al., 2012). All dates are reported with analytical uncertainties at the 95 % confidence level.

## 4 Results and discussion

### 4.1 Performance differences between PFIB and femtosecond laser machining

Our tests confirm that machining footprint and speed are the main performance differences between the PFIB and femtosecond laser. $Xe^+$ and $Ar^+$ PFIBs offer clean machining with no surface debris and produce sharp cuts with machining precision on the order of ∼ 8–20 µm (for commonly used 0.5–2.5 µA ion beam currents). Thanks to these features, the PFIB is particularly suited for machining of microsamples of small (20 µm) to moderate (100 µm) dimensions, where the required machining times range between ∼ 45 min and ∼ 3 h. The applicability of the PFIB is reduced for larger microsamples (≫ 150 µm), where the cumulative machining time becomes prohibitively long. For such applications, faster machining with the femtosecond laser ($>10\,000\,\mu m^3\,min^{-1}$ compared to $<1000\,\mu m^3\,min^{-1}$ for PFIB) is preferred, either for microsampling from start to finish or at least for initial trenching of large material volumes. In general, with its larger beam size (≥ 20 µm), rough cuts, and more invasive machining footprint, femtosecond laser machining is arguably already too crude for most microsample sizes expected in future studies on natural zircon ($\leq 100 \times 100 \times 100\,\mu m^3$). Compared to the nanosecond laser, the femtosecond laser does not produce severe topography and surface debris (White et al., 2021). On the Laser Hydra instrument used here, femtosecond laser machining requires mounting of zircon in smaller-radius (∼ 1 cm) mounts on a pre-tilted (54°) holder to achieve full flexibility of machining angles.

### 4.2 Microsampling-induced structural damage in zircon

Damage caused by the $Xe^+/Ar^+$ ion beam (PFIB) and femtosecond laser microsampling was tested in a series of irradiation experiments on centimeter-sized, carbon-coated Mud Tank crystals (Figs. S5–S7). Each irradiation employed a normal-incidence ion beam and targeted zircon zones of homogeneous cathodoluminescence texture to minimize crystal heterogeneity effects. The PFIB irradiation experiments were carried out at voltage conditions ranging from 3 to 30 kV to assess damage during both fine ion polishing (low voltage) and rough machining (high voltage; Figs. S5 and S6). In each experiment, the ion beam current was adjusted to the best-fitting discrete current option for consistency between the ion species ($Xe^+$ versus $Ar^+$) and different instruments (Fera3 versus Hydra). To balance the reduced material removal rate at low voltages (3 and 5 kV), the ion dose was increased such that the exposed region was milled. This ensures that the produced damage is representative, i.e., corresponds to the damage generated on the walls of a microsample prepared by ion milling. PFIB-induced structural damage was analyzed on cross-sections (i.e., TEM lamellae) from the top surface in normal-incidence experiments. Additionally, we analyzed a side wall of a $Xe^+$-PFIB-machined microsample of Mud Tank zircon to test how representative our ion irradiation experiments are of the microsampling procedure (Fig. S8). Femtosecond laser irradiation was performed on an embedded zircon with one side exposed (i.e., edge sample) by cutting the mount laterally with a micro-saw (Fig. S7). The exposed edge was irradiated with the femtosecond laser beam oriented parallel to the edge, employing a 515 nm wavelength configuration with vertical polarization, a 60 kHz repetition rate, 0.96 W power, and a pulse energy of 16 µJ.

Our experiments show that PFIB machining produces a topmost amorphized damaged zone that hosts a layer of implanted ions (Figs. 3, 4, and S9–S11). The thickness of this damaged zone, as well as the depth and thickness of the ion-implanted layer, increases from <1 nm to a few tens of nanometers with increasing ion beam voltage (3 to 30 kV). At the maximum 30 kV ion beam voltage, which we apply for microsampling, $Xe^+$ irradiation produces a somewhat thinner (∼ 50 nm for Fera3 and ∼ 40 nm for Hydra) damaged layer compared to $Ar^+$ (∼ 60 nm), making $Xe^+$ the preferred ion species for zircon microsampling. Irrespective of the ion species and applied voltage, the damaged zone exhibits a porous, spongy texture (Figs. S7–S9). The transition towards the underlying undamaged zircon is marked by a change from amorphous to crystalline matter displaying periodic arrangement of atoms in high-resolution TEM images (Figs. 4, S10 and S11). At the highest energies (15 and 30 kV), the damaged zone exhibits swellings associated with local enrichments in Zr and Si and depletion in O.

Femtosecond laser machining damages zircon over micrometer length scales that for smaller microsamples correspond to their entire volume (Figs. 3, 4i–n, and S12). The laser-irradiated zircon is porous and exhibits fractures and globular (melt?) structures over the entire extent of the TEM lamellae. In the topmost domains of the TEM lamellae immediately exposed to irradiation, Zr is depleted and Si is enriched in increasingly porous domains. The globular structures (100–500 nm wide), as well as most of the irradiated zircon, appear amorphous, with crystalline structure detectable only locally in 0.5–1 nm wide patches.

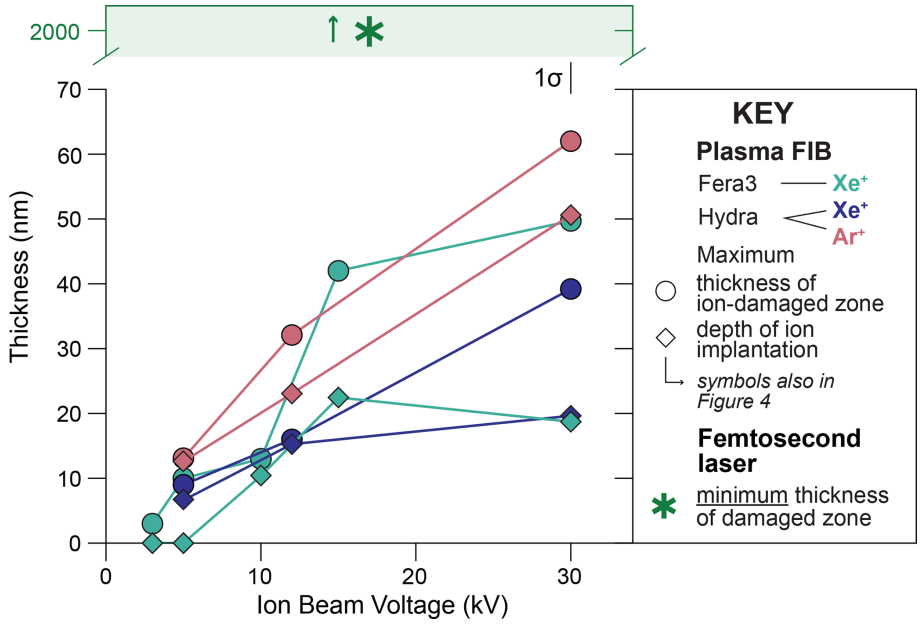


**Figure 3.** Structural damage in zircon induced by irradiation with the plasma focused ion beam ($Xe^+$ and $Ar^+$) and femtosecond laser. PFIB damage is quantified in terms of the maximum thickness of the damaged zone and maximum depth of ion ($Xe^+/Ar^+$) implantation. The minimum thickness of the zone damaged by the femtosecond laser irradiation is at least 2 orders of magnitude higher than that generated by the PFIB (tens of nanometers versus >2 µm).

### 4.3 U–Pb systematics of zircon microsamples

#### 4.3.1 Impacts of Pt–Pd and Cr coating

Thin metal coatings (<20 nm) are commonly used in PFIB machining to reduce beam drift (i.e., deviation of the true compared to the projected machining pattern), whereas thicker electron or ion beam deposited caps (>20 nm) are typically used to protect the underlying material from damage caused by the ion beam tails when machining the material adjacent to the cap (Ishitani and Yaguchi, 1996). Since the amounts of sample Pb and U in dated zircons are small (pg–ng), it is critical that any additional U or Pb contributions from the coating prior to microsampling can be avoided or corrected for. We tested the impact of Pt–Pd (8 : 2) and Cr protective coatings (both 99.95 % purity) on U–Pb systematics with high-precision (CA-ID-TIMS) U–Pb isotope analyses carried out on both metal- and carbon-coated whole zircon crystals undergoing the same preparation steps (Table S2). Carbon-coated crystals served as a benchmark group. The ∼ 0.63 Ma Lava Creek Tuff Unit A (LCT-A; Wotzlaw et al., 2015) and ∼ 3467 Ma Owens Gully Diorite (OG-1; Kemp et al., 2017; Stern et al., 2009) zircon were chosen as young, U-rich, and Pb-poor and old, U-poor, and Pb-rich end-members, respectively (Figs. S1 and S13). Importantly, for both samples, all individual zircon dates acquired so far by CA-ID-TIMS using an EARTHTIME tracer solution overlap within uncertainty (Wotzlaw et al., 2015; Laurent et al., 2020), which allows identifying excess dispersion introduced by the coating. A first random selection of crystals from both zircons was imaged by CL-SEM to assess within-sample textural variability (Fig. S13). Subsequently, a second random selection of crystals was hand-picked and separated into three aliquots, with care taken to avoid bias based on crystal size and habit. Each was mounted in epoxy, and the exposed surfaces of the first two aliquots were coated with a 20 nm layer of Pt–Pd and Cr, while the third aliquot was coated with 20 nm of carbon.

We find no systematic bias in U–Pb systematics of metal-coated zircon compared to the benchmark zircon coated with carbon (Fig. 5). For the LCT-A zircon, the $^{230}$Th-corrected $^{206}Pb/^{238}U$ dates of the Pt–Pd- and Cr-coated as well as the carbon-coated zircon all overlap within uncertainty at ∼ 0.63 Ma, and each group yields weighted mean dates equivalent to those of Wotzlaw et al. (2015). Pt–Pd-coated crystals show somewhat higher common Pb masses ($Pb_c$) of 0.39 ± 0.12 pg (mean ± 1 SD) compared to 0.12 ± 0.05 pg for C-coated crystals, while the Cr-coated crystals (0.27 ± 0.14) are indistinguishable from the two groups (Fig. 5b). The U–Pb analyses of the metal- and carbon-coated aliquots of the OG-1 show discordance with a broad zero-age intercept, consistent with present-day Pb loss or cryptic U-blank effects (see later in the text). The $^{207}Pb/^{206}Pb$ dates plateau at ∼ 3466.4 Ma, consistent with the results of Laurent et al. (2020; Fig. 5a). A few younger $^{207}Pb/^{206}Pb$ dates, between 3464–3466 Ma, are recorded for crystals chemically abraded at 190 °C irrespective of the applied coating, which is suggestive of leaching-induced isotopic fractionation resulting from insufficient du-

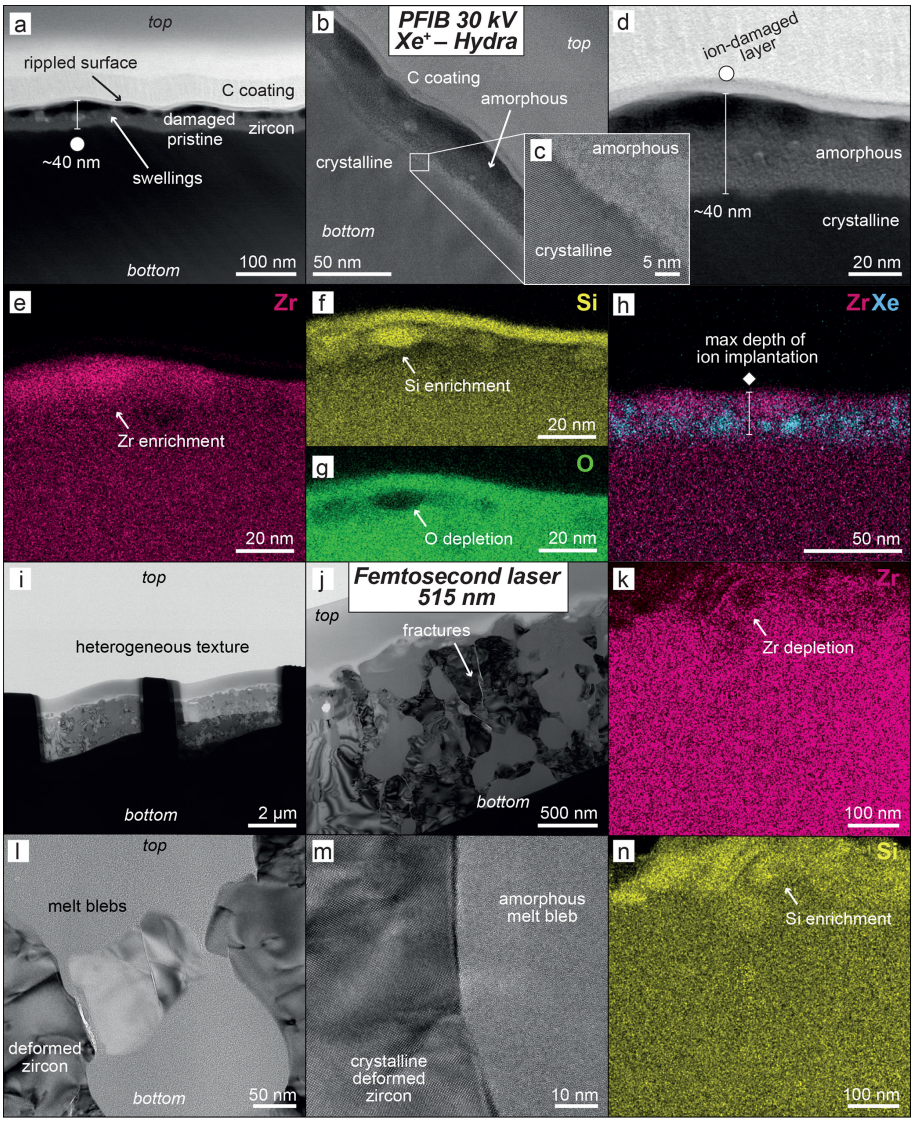


**Figure 4.** **(a–h)** Transmission electron microscope (TEM) images of the uppermost PFIB-damaged zone. The damaged zircon is porous and amorphous and shows local swellings. **(e–h)** EDS maps of the PFIB-damaged zone showing surface enrichment of Zr and Si and relative depletion of O. **(h)** Implanted layer of $Xe^{+}$ within the damaged zone. **(i–n)** TEM images showing the chaotic texture of zircon damaged by femtosecond laser irradiation. The damaged zone is fractured and contains globular structures (melt?) with only locally preserved crystalline domains **(i, j, l, m)**. Zr is depleted **(k)** and Si is enriched **(n)** in the uppermost zone immediately exposed to laser irradiation.

ration or temperature of chemical abrasion (McKanna et al., 2024). The equivalent common Pb mass ($Pb_c$) for OG-1 zircon coated with metal ($0.27 \pm 0.10$ pg for Pt–Pd and $0.28 \pm 0.10$ pg for Cr) and carbon ($0.37 \pm 0.07$ pg), together with overlapping dates for different groups of both LCT-A and OG-1 zircon, indicates that any contribution of Pb from the metal, if present, was efficiently removed during chemical abrasion at both 190 and 210 °C. The different coating groups are also indistinguishable in terms of total (sample + blank) U mass (Fig. 5f). The metal-coated crystals subjected to chemical abrasion at 190 °C yield on average higher total U mass (up to 500 pg) compared to the ones abraded at 210 °C (<250 pg), in line with the greater amount of dissolution of high-U zones observed at higher chemical abrasion temperatures (McKanna et al., 2024). Since no measurable effect of coating material on Pb and U mass was observed, in our further microsampling work we only applied carbon coating. This allowed us to shorten sample preparation time (i.e., skip repolishing and coating with metal prior to microsampling) and to make use of CL-SEM imaging in between machining steps. Occasional beam drift ($\ll 20$ µm) experienced when working with carbon coating only was mitigated by re-coating the mount with a new 20 nm layer of C after $\sim 20$ h of PFIB machining.

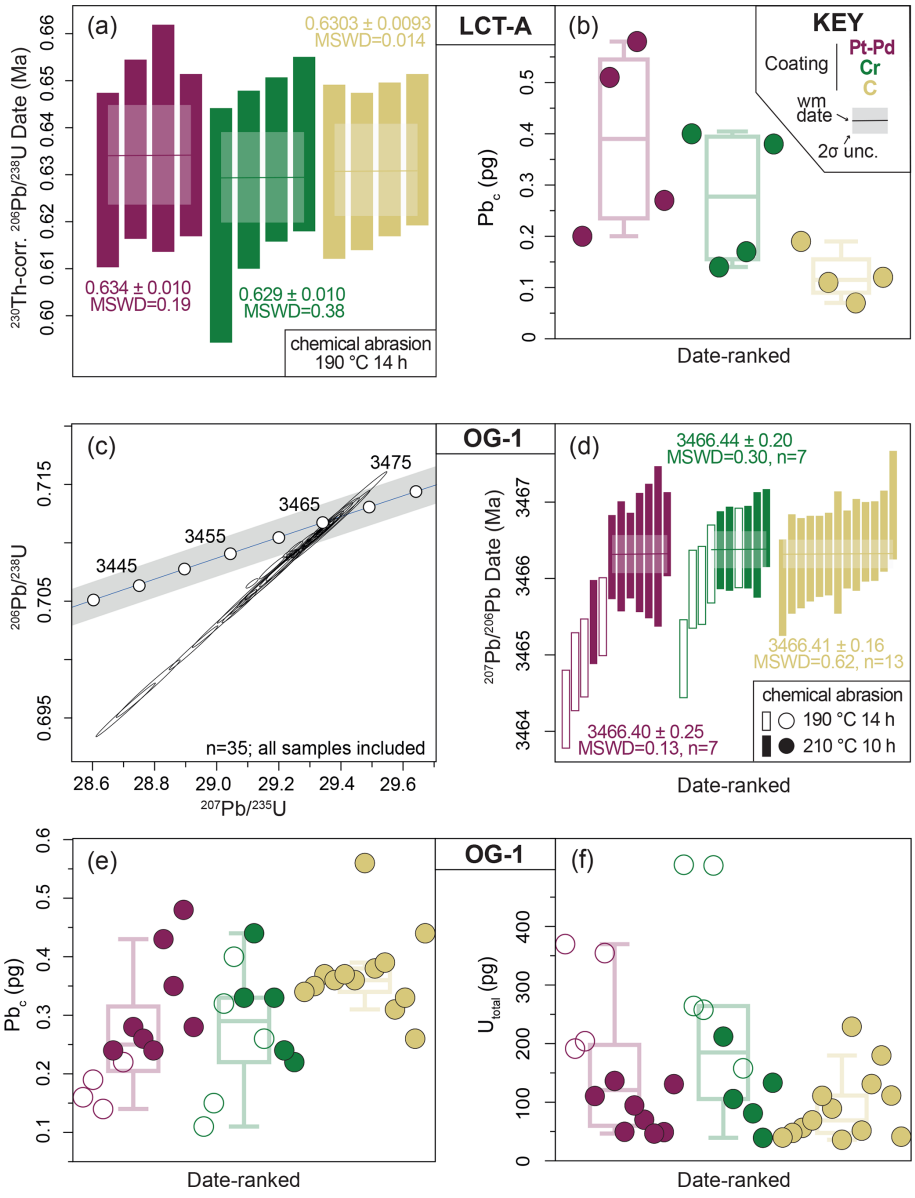


**Figure 5.** U–Pb systematics of **(a–b)** Lava Creek Tuff Unit A (LCT-A) and **(c–f)** Owens Gully Diorite (OG-1) zircon coated with metal (Pt–Pd and Cr) and carbon. All uncertainties are quoted at the $2\sigma$ level. $Pb_c$ is the mass of common Pb, and $U_{total}$ is the mass of U from the sample and blank.

### 4.3.2 High-precision U–Pb isotope systematics of PFIB and femtosecond laser zircon microsamples

A total of 27 microsamples of Mud Tank and GZ7 zircon machined with the $Xe^+$ PFIB and femtosecond laser were prepared for CA-ID-TIMS U–Pb analysis (Fig. 6 and Table S2). To explore the effect of microsample size (i.e., microsamples' mass of radiogenic lead – $Pb^*$ and U) and PFIB/femtosecond laser irradiation on the accuracy and precision of µID-TIMS dates, we machined microsamples covering a range of sizes from $40 \times 18 \times 40$ to $100 \times 80 \times 70\,\mu m^3$. Besides microsamples, we also analyzed thermally annealed, non-machined large pieces and shards of crushed Mud Tank and GZ7 zircon as a benchmark group of large and small non-irradiated aliquots.

Our analyses of the large pieces of the U-poor (9 ppm) Mud Tank zircon were concordant with $^{206}Pb/^{238}U$ dates between 708–711 Ma, which we consider a reference for the microsample analyses (Fig. 6e). Note that our analyses yield dates up to 20 Ma younger than the ones published in the literature (Fig. 5e; Black and Gulson, 1978; Jain et al., 2001; Horstwood et al., 2016; Gain et al., 2019), which may be due to isotopic variability of individual Mud Tank megacrysts, similar to what Schaltegger et al. (2015b) observed for zir-

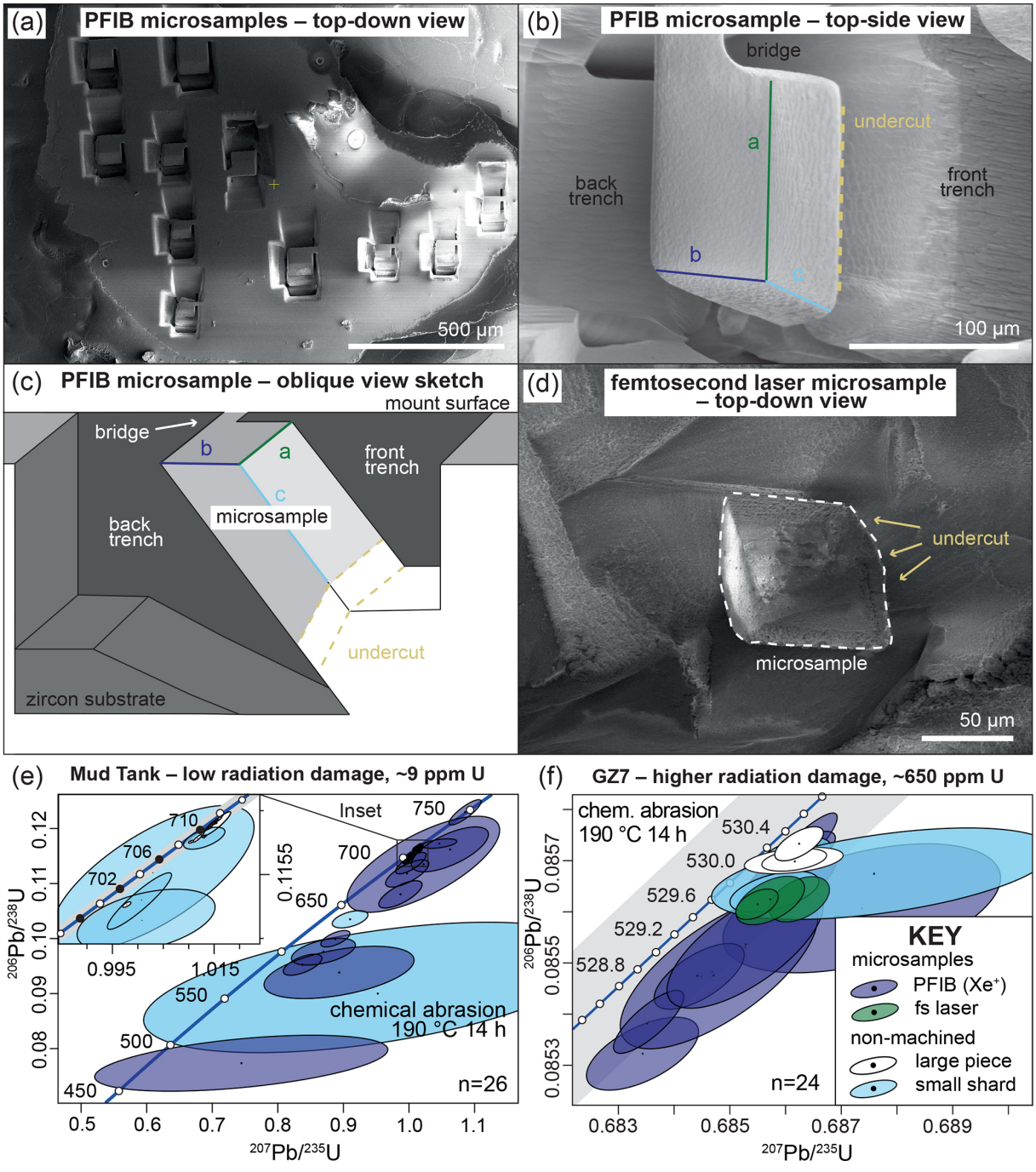


**Figure 6.** Geometry and high-precision U–Pb isotope systematics of PFIB- and femtosecond-laser-machined microsamples of Mud Tank and GZ7 zircon. **(a)** A total of 11 PFIB microsamples ($\sim 40 \times 18 \times 40$–$100 \times 80 \times 70\,\mu m^3$) within a single crystal of GZ7 zircon. **(b)** SEM image and simplified sketch **(c)** of a finalized microsample machined with the $Xe^+$ PFIB. **(d)** Top-down view of a femtosecond-laser-machined microsample. **(e–f)** U–Pb isotope systematics of PFIB and femtosecond laser microsamples of Mud Tank and GZ7 zircon compared with non-machined larger pieces and smaller shards.

con megacrysts from the Alps. Results for PFIB microsamples and small shards of Mud Tank have larger uncertainties than those of large pieces, which is explained by their much smaller sizes and resulting lower radiogenic to common Pb ratios (<25 compared to 230–2260). The microsamples and non-irradiated small shards plot along a discordant array extending from a few concordant points between ~ 700–745 Ma towards a broadly defined zero-age lower intercept (Fig. 6e), consistent with heterogeneous Pb loss or U gain.

For the GZ7 zircon (~ 650 ppm U), our analyses of large pieces are concordant at 529.93 ± 0.07 Ma ($^{206}Pb/^{238}U$ date; Fig. 5f), providing a reference date in agreement with the literature (Fig. 5f; Nasdala et al., 2018). PFIB microsamples of GZ7 zircon are also concordant, with some overlapping with the large reference pieces at 529.9 Ma and others spreading towards younger dates that overlap with the uncertainty of the concordia but describe an array similar to that seen in the Mud Tank data. From the five microsamples prepared with the femtosecond laser, the two largest pieces ($110 \times 105 \times 60$ and $75 \times 70 \times 45\,\mu m^3$) were preserved during chemical abrasion at 190 °C; one disintegrated into shards ($65 \times 45 \times 35\,\mu m^3$), while the two smallest microsamples ($55 \times 55 \times 40$ and $50 \times 25 \times 30\,\mu m^3$) were fully dissolved. We interpret the dissolution of the smallest microsamples to be caused by femtosecond-laser-induced amorphization that for the smaller-volume microsamples may affect their entire volume. The three analyzed femtosecond laser microsamples were also concordant, partly overlapping with the PFIB microsamples, but on average younger than the large pieces at 529.6 Ma. Three analyses of non-irradiated small shards of GZ7 overlap with the large reference pieces and femtosecond laser microsamples, as well as with the older PFIB microsamples.

The observed spread for PFIB and femtosecond laser microsamples compared to reference pieces may reflect the natural age heterogeneity of the GZ7 crystal on a micrometer scale, or it is an analytical artifact. The former is unlikely given consistent $^{206}Pb/^{238}U$ dates of GZ7 at ~ 530 Ma reproduced by four laboratories (Nasdala et al., 2018). We identify two analytical causes that may explain the spread towards younger dates: PFIB- or femtosecond-laser-induced Pb loss or underestimated U blank.

We speculate that some Pb loss may occur from the outermost zones of the zircon microsamples damaged during PFIB and femtosecond laser machining (additional heat effect). If not mitigated during chemical abrasion, this would affect the U–Pb isotope data of our microsamples proportionally to the extent of the damaged volume. We computed the PFIB- and femtosecond-laser-damaged volume proportion of zircon microsamples, excluding the top surface, which was not machined. $^{206}Pb/^{238}U$ offset – deviation from accurate dates – for individual microsamples and non-irradiated zircon (i.e., large pieces and shards) was calculated as the relative difference from the average composition of the large pieces for

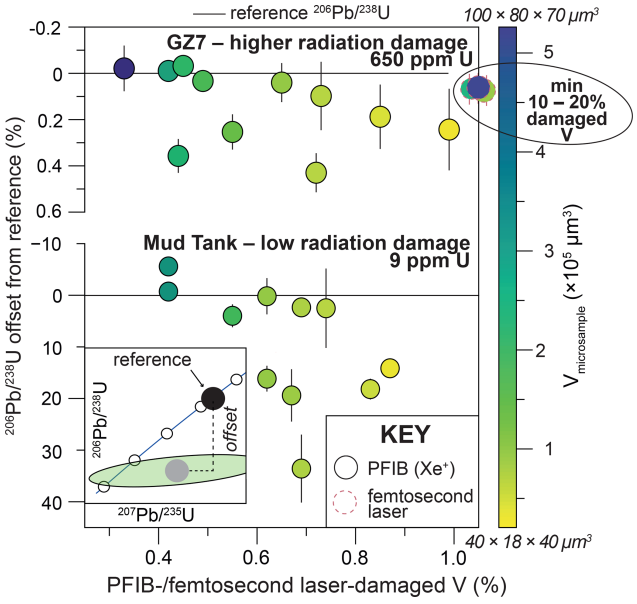


**Figure 7.** $^{206}Pb/^{238}U$ offset (deviation from accurate dates) versus relative microsample volume damaged by PFIB and femtosecond laser machining. The minimum volume damaged by the femtosecond laser is on the order of 10 %–20 % compared to <1 % for PFIB. Note that the thickness of the damaged zircon zone is constant (39 nm for $Xe^+$ PFIB and a minimum of 2 µm for the femtosecond laser) and translates into proportionally larger damaged volumes for smaller microsamples. The dimensions (a × b × c in Fig. 6b and c) of the smallest and largest PFIB microsample are given for reference.

Mud Tank and GZ7 zircon. For this exercise, we assume no dissolution of the damaged zone during chemical abrasion despite evidence for dissolution of smaller femtosecond laser microsamples. Figure 7 shows a weak correlation between $^{206}Pb/^{238}U$ offset and the damaged volume for PFIB and no correlation for femtosecond microsamples. For the GZ7 zircon (~ 650 ppm U, higher radiation damage), the $^{206}Pb/^{238}U$ and damaged volume of PFIB microsamples show comparable values on the order of <1 %, and similar small offsets values are recorded for femtosecond laser microsamples despite the damaged zone occupying >10 % of their volume. For the U-poor (~ 9 ppm, low radiation damage) Mud Tank zircon, the offset values reach 35 % for similar damage volumes, suggesting that the magnitude of offset (degree of inaccuracy) is controlled by a factor specific to each zircon sample. Importantly, these observations imply that PFIB/femtosecond laser machining prior to ID-TIMS zircon analyses does not introduce a systematic bias into U–Pb dates.

Still, within each group (Mud Tank vs. GZ7 zircon, PFIB vs. femtosecond laser microsamples), the $^{206}Pb/^{238}U$ offset is correlated with microsample size, with smaller microsamples being more strongly offset (Fig. 7). Extending the analysis to non-microsampled zircon (large pieces, shards, and whole crystals), we observe that the offset is greatly in-

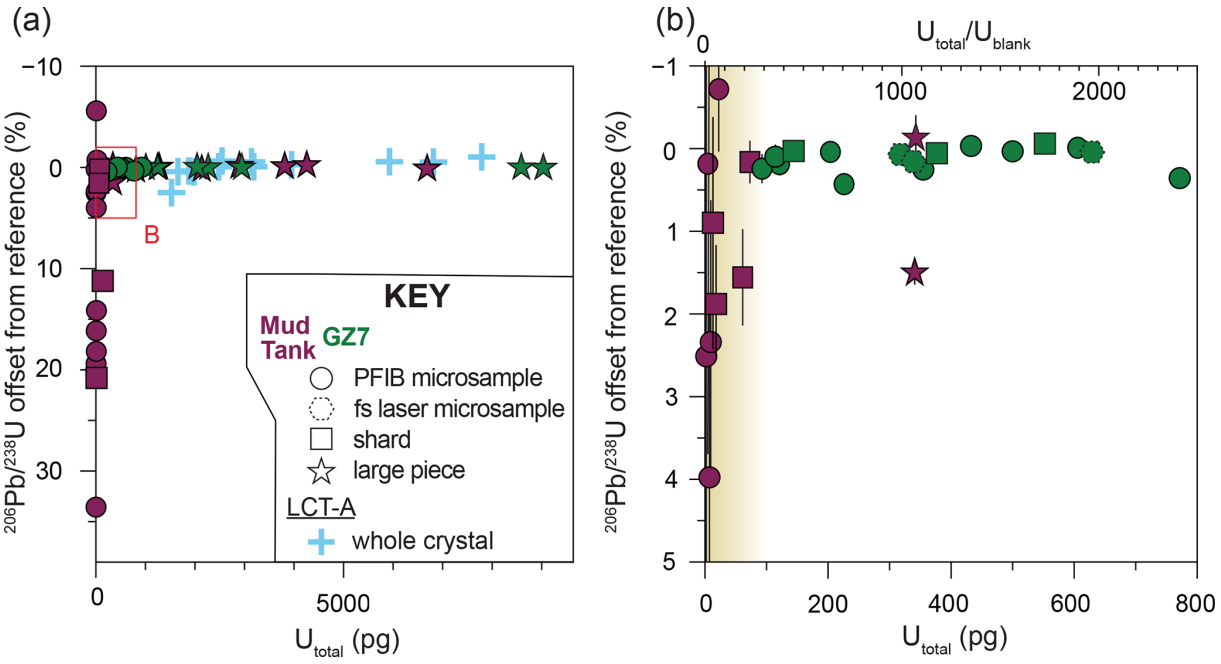


**Figure 8.** $^{206}Pb/^{238}U$ offset as a function of total U mass analyzed (sample + blank) and in relation to U-blank mass (fixed at $0.32 \pm 0.08$ pg). The offset values increase exponentially to percent levels (<35 %) for both PFIB and femtosecond laser microsamples, as well as non-machined zircon for $U_{total}/U_{blank}$ below ~ 300. Residual <1 % offsets observed for $U_{total}/U_{blank}$ are due to heterogeneities in the U–Pb isotope composition of dated zircon aliquots, unmitigated Pb loss, or unresolved U-blank effects.

creased (<35 %) for low-U-mass (sample + blank) analyses (<160 pg U), whereas higher-U-mass analyses are less offset (mostly below <1 %; Fig. 8). This observation is consistent with inaccuracies being controlled by isotopic mixing of zircon U isotopic composition with that of the laboratory blank U. Assuming for this purpose that blank U has $^{238}U/^{235}U$ of $137.818 \pm 0.045$ representative of magmatic zircon (Hiess et al., 2012), we find that individual Mud Tank microsamples, prepared within a single batch of analyses, require $U_{blank}$ mass between −0.12 and 1.94 pg to force concordance at our reference age of 711 Ma (Fig. S14a). Such U-blank masses agree in magnitude with our analyses of total procedural blanks from the period over which this study was conducted ($n = 20$), which returned a mean value of $0.32 \pm 0.08$ pg (1 SD) and several outliers reaching >1 pg U (Fig. S14b). The presence of such extreme outliers, as well as the high-U blanks implied by the most offset Mud Tank results, suggests a source of U in our analyses that is highly variable. We find that reagent and loading U blanks are generally low and reproducible (0.12–0.23 pg U; Fig. S14b) and tentatively link the random, elevated blanks to memory effects of re-used PFA labware (e.g., microcapsules used to dissolve zircon grains). The $U_{blank}$ mass may therefore be an underappreciated source of random uncertainty, calling for systematic monitoring and mitigation, especially prior to analyses of low-total-U-mass zircon (microsamples and whole crystals). Smaller residual offsets on the order of <1 %, observed for GZ7 microsamples as well as non-machined zircon, arguably reflect heterogeneities in U–Pb isotope composition, minor unmitigated Pb loss, or still unaccounted for U-blank effects. For zircon microsamples, as for non-machined zircon, it follows that for a given laboratory U blank (mass and isotope composition) and zircon of a certain age and U concentration, the $U_{total}/U_{blank}$ and therefore U–Pb accuracy become chiefly dependent on microsample size.

### 4.4 Designing a µID-TIMS study: minimum zircon microsample size

High-precision U–Pb geochronology of zircon microsamples (µID-TIMS) can be applied to zircon of all ages and U concentrations due to the negligible effects of the microsampling procedures on the U–Pb systematics. As microsample size, U concentration, and age determine the total mass of U and radiogenic Pb* for any zircon and these parameters limit the attainable precision of the U–Pb analysis, knowing how small a zircon microsample can be prior to analyses is crucial for planning a successful µID-TIMS study. This is particularly true considering the substantial time and cost factors involved in PFIB microsampling. The ability to precisely and accurately date zircon microsamples also critically depends on the mass and isotopic composition of Pb and the U laboratory blank, which should be well characterized in order to plan and execute such a study.

Figures 9 and 10 display the impact of microsample size on the resulting $U_{total}$ and $Pb^*/Pb_c$ for zircon covering a range of U concentrations and age. Given the U blanks measured over the course of this study, an example microsample of $50 \times 50 \times 50\,\mu m^3$ requires a minimum U concentration of $\sim 250$ ppm to become relatively insensitive to U-blank correction, while low-U ($\sim 50$ ppm) zircon microsamples require a minimum size of $\sim 80 \times 80 \times 80\,\mu m^3$ ($U_{total}/U_{blank} > 300$; Fig. 9). Importantly, if the U blank is accurately constrained and corrected for (long-term and within-chemistry $U_{blank}$ mass and isotopic composition, if possible), U-blank correction does not impose a limit on the accuracy of µID-TIMS dates. This is particularly important for $^{206}Pb/^{238}U$ dating of the smallest microsamples ($\sim 20 \times 20 \times 20\,\mu m^3$). For old zircons, where $^{207}Pb/^{206}Pb$ dates are used, the mass of the U blank ($U_{total}/U_{blank}$) is important to evaluate concordance, while its isotopic composition is used to calculate Pb–Pb dates. For Pb, assuming a constant laboratory Pb-blank mass (here 0.1 pg $Pb_c$), the minimum microsample size and $Pb^*/Pb_c$ are a function of age and U content. Taking as an example $Pb^*/Pb_c = 20$, which represents a minimum ratio where Pb-blank correction becomes a minor source of uncertainty (Schoene and Baxter, 2017), relative uncertainty in $^{206}Pb/^{238}U$ on the order of 0.1 % can be achieved for moderate to large microsamples ($>80 \times 80 \times 80\,\mu m^3$) of older (>500 Ma) zircon richer in uranium ($\geq 500$ ppm; Figs. 10 and 11). It is noteworthy that regardless of their U concentration, for small microsamples of young zircon (<20 Ma) with low $Pb^*/Pb_c$, Pb-blank correction is the main contributor to the total analytical uncertainty in $^{206}Pb/^{238}U$ dates, but the absolute precision can still be sufficient to resolve studied processes at these ages. Another consideration may be alpha recoil that acts over submicrometer length scales (Nasdala et al., 2001; Romer, 2003; Davis and Davis, 2018), which in small and high-aspect-ratio microsamples extracted from zircon grains strongly zoned in U may lead to Pb excess or deficit in the microsampled volume. Whether this would result in resolvable inaccuracies in U–Pb systematics needs to be quantified.

To predict these parameters for each case, we developed an open-source code written in Python that builds on zircon age, composition (estimated or measured U and Th concentrations), and microsample volume, as well as laboratory $U_{blank}$ and $Pb_c$, to compute the expected $U_{total}/U_{blank}$ and $Pb^*/Pb_c$ of the analysis. These ratios are then evaluated against threshold $Pb^*/Pb_c$ and $U_{total}/U_{blank}$ in the case of $^{206}Pb/^{238}U$ dates, and, if lower, a new minimal microsample volume satisfying both conditions is returned. Estimating the precision of a future microsample date is done by comparing the computed $Pb^*/Pb_c$, which is the best predictor of achievable analytical precision, with a compilation of literature CA-ID-TIMS U–Pb and Pb–Pb zircon dates (Fig. 11; see the database in the Supplement). For different $Pb^*/Pb_c$ values (0.1–10 000), the best achievable precision ranges from <10 ka for Cenozoic zircon to between 0.1–1 Ma for older

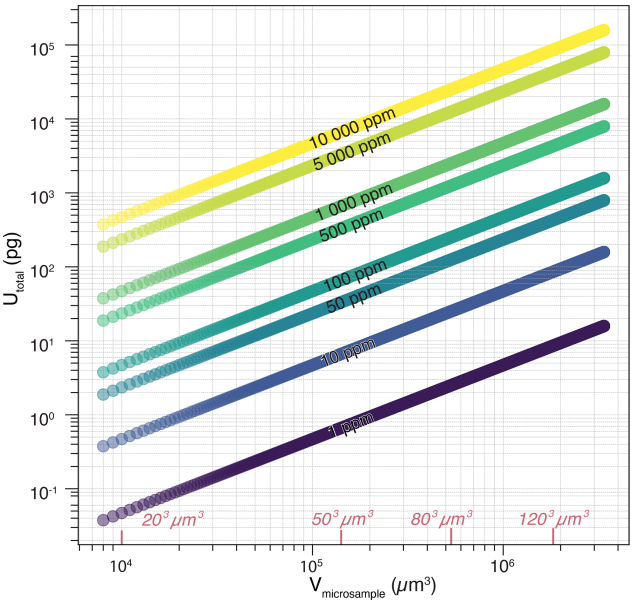


**Figure 9.** Microsample U mass ($U_{total}$) as a function of microsample volume and zircon U concentration (1–10 000 ppm). Volumes corresponding to cubes of 20, 50, 80, and 120 µm side dimensions are given for reference.

zircon (mostly <0.1 %–2 % and <12 % for Quaternary zircon).

### 4.5 Outlook and potential

µID-TIMS introduces spatially resolved high-precision U–Pb geochronology. It combines the accuracy and precision achievable by ID-TIMS with the spatial control of in situ techniques. This methodology can be broadly applied to tackle a variety of questions related to age determination and timescales not previously accessible for direct quantification. These include (1) paired core-and-rim dating to constrain rates of zircon growth across different magmatic environments, (2) dating of the outermost rims of volcanic zircon to more accurately constrain ages of volcanic eruptions, (3) analysis of young rims in zircon from high-temperature metamorphic terranes to quantify timescales of crustal melting and zircon crystallization, (4) extraction of whole zircon or microsamples from thin sections for high-precision geochronology with petrographic context, (5) dating of precious zircon from meteorites or samples from sample return space missions to investigate timescales of protoplanetary processes, and (6) investigation of heterogeneities in U–Pb systematics in zircon reference materials on the scale of single crystals. Beyond zircon, PFIB and femtosecond laser machining may replace microdrilling as a more precise method for obtaining texturally controlled aliquots of complex samples for isotopic analyses, as well as being applied to microsampling of other U-bearing accessory minerals such as titanite, rutile, apatite, and baddeleyite and to other radio-

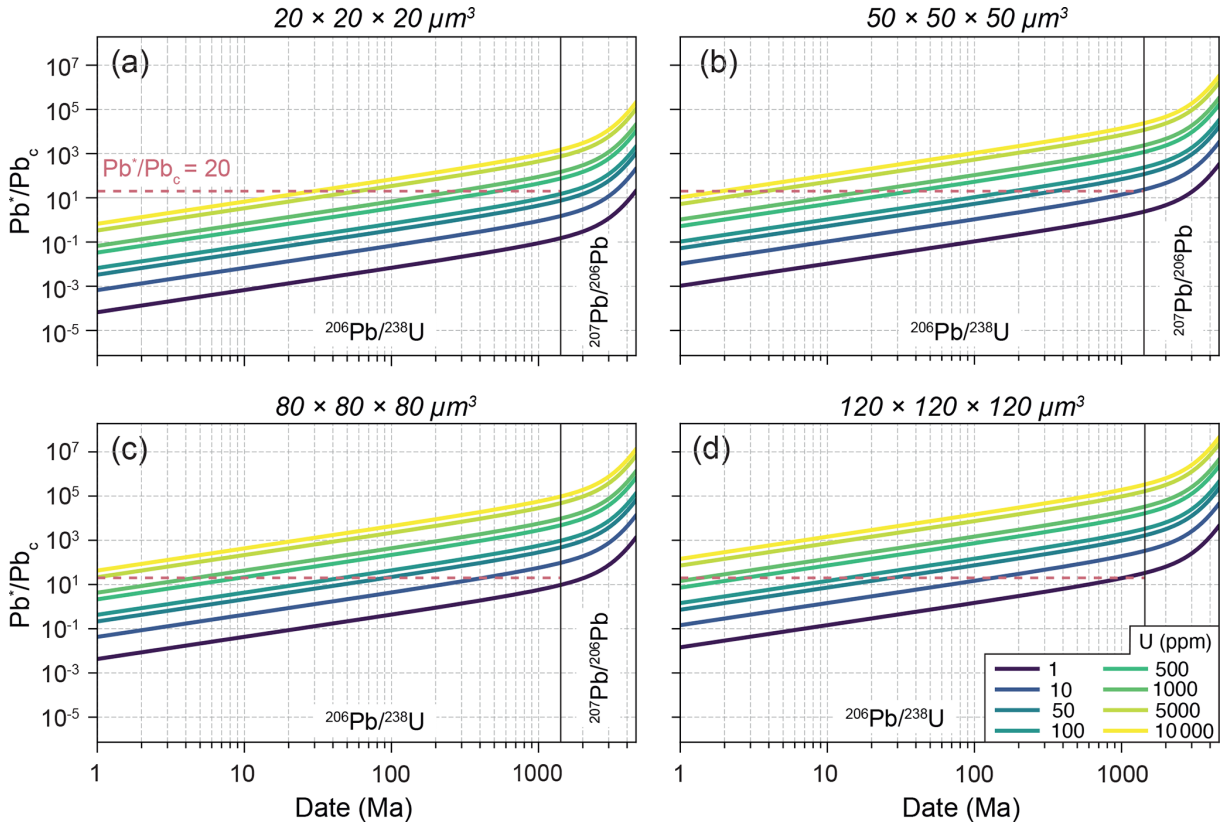


**Figure 10.** Theoretical radiogenic to common Pb ratios ($Pb^*/Pb_c$) for microsamples of different size machined from zircon covering a range of ages and U concentration (1–10 000 ppm). All models assume a laboratory Pb blank ($Pb_c$) of 0.1 pg. $Pb^*/Pb_c = 20$ marks the empirical threshold below which the Pb-blank correction dominates the analytical uncertainties in $^{206}Pb/^{238}U$ dates (Schoene and Baxter, 2017).

genic or stable isotope systems. The microsampling workflow could further be improved through volume imaging of internal zircon growth zones in absolute space coordinates to fully automate the machining process.

## 5 Conclusions

We presented a novel, plasma focused ion beam (PFIB)–femtosecond (fs) laser–CL-SEM machining methodology for microsampling of zircon fragments for spatially resolved, high-precision U–Pb geochronology (µID-TIMS). Our machining experiments and tests of the impact of the microsampling methodology on U–Pb systematics of CA-ID-TIMS-dated zircon microsamples led to the following findings.

1. PFIB ($Xe^+/Ar^+$) is the preferred tool for machining of microsamples of small to moderate dimensions (∼ 20 to 120 µm length scale). Microsamples of these sizes are machined with PFIB within times between ∼ 45 min and 3 h.

2. Femtosecond laser machining is more time- and cost-effective for larger microsamples (> 120 µm), especially for applications in which the lower beam precision (≥ 20 µm), micrometer-scale induced structural damage, and overall larger surface footprint are not a concern – including applications other than zircon U–Pb geochronology.

3. Machining with PFIB can be performed on zircon with protective metal (Pt–Pd and Cr) coating or standard carbon coating without introducing any bias to the U–Pb systematics.

4. PFIB and femtosecond laser machining followed by chemical abrasion do not introduce systematic inaccuracies into U–Pb systematics of the analyzed microsamples.

5. Analyzing smaller microsamples (low mass of radiogenic Pb and U) accurately and at high precision critically depends on Pb and U blanks. We propose that reporting of long-term and within-chemistry Pb and U blanks (mass and, if possible, isotopic composition) therefore be considered a standard data reporting procedure in future microsampling studies.

6. PFIB–femtosecond laser microsampling for high-precision U–Pb geochronology can be applied to zir-

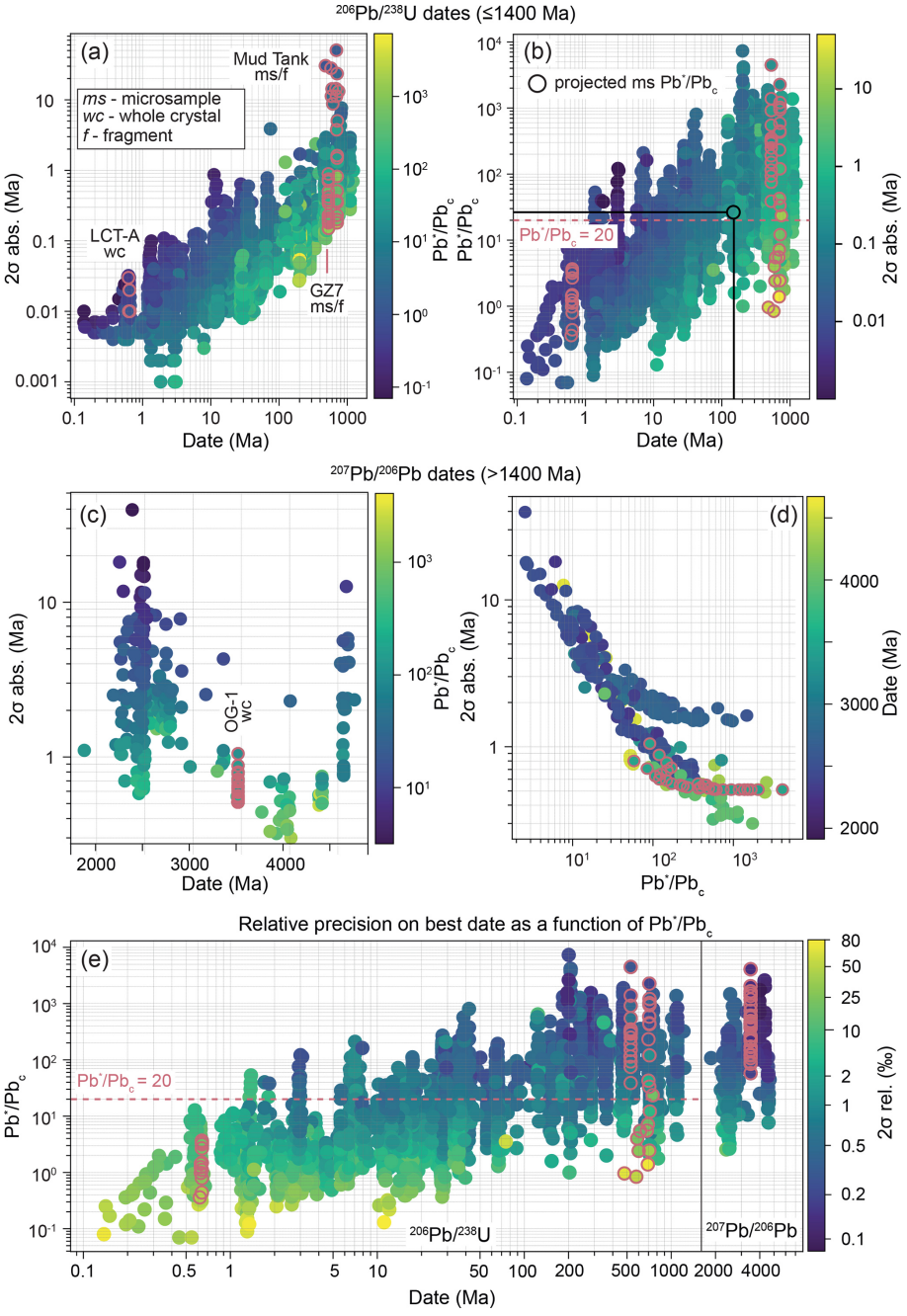


**Figure 11.** Achievable $2\sigma$ analytical precision on ID-TIMS $^{206}Pb/^{238}U$ **(a–b)** and $^{207}Pb/^{206}Pb$ **(c–d)** dates of microsamples as a function of zircon age and measured $Pb^*/Pb_c$ based on a large compilation of ID-TIMS U–Pb geochronology results (see the database in the Supplement). For a zircon of given age and U concentration, as well as known laboratory $Pb_c$ levels (here 0.1 pg), microsample size alone determines $Pb^*/Pb_c$. Panel **(b)** shows an example of a projected $Pb^*/Pb_c$ for a $50 \times 50 \times 50\,\mu m^3$ microsample of a 150 Ma zircon with 250 ppm U. In **(e)**, the best date is defined as $^{206}Pb/^{238}U$ date for ages $\leq$ 1400 Ma and $^{207}Pb/^{206}Pb$ for >1400 Ma. Symbols with red outlines are samples analyzed in this study.

con of any age and U concentration. As for bulk-grain geochronology, the achievable precision is a function of $U_{total}/U_{blank}$ and $Pb^*/Pb_c$, which in turn depend on zircon microsample size, age, U concentration, and laboratory blank. Our open-access code can aid researchers in evaluating these parameters in target zircons and assessing in advance whether the achievable analytical precision can resolve the expected timescales of studied processes.

µID-TIMS introduces a new, spatially resolved, high-precision U–Pb zircon dating method, bridging the gap between conventional bulk-grain and in situ dating. Our method opens a number of new applications in Earth and planetary sciences.

**Code and data availability.** Original analytical data, compilation of ID-TIMS dates, and the code presented in this study are available in the Supplement.

**Supplement.** The supplement related to this article is available online at: https://doi.org/10.5194/gchron-6-621-2024-supplement.

**Author contributions.** SM collected the data presented in this manuscript, prepared the figures, and wrote the manuscript with input from all co-authors. DS, JR, and PZ assisted with the data collection and provided input during manuscript writing. Discussion of the data involved all authors. CCM and JFW designed and obtained funding for the study. CCM supervised the study.

**Competing interests.** The contact author has declared that none of the authors has any competing interests.

**Disclaimer.** Publisher's note: Copernicus Publications remains neutral with regard to jurisdictional claims made in the text, published maps, institutional affiliations, or any other geographical representation in this paper. While Copernicus Publications makes every effort to include appropriate place names, the final responsibility lies with the authors.

**Acknowledgements.** We acknowledge the Scientific Center for Optical and Electron Microscopy (ScopeM) of ETH Zurich for providing critical analytical resources for conducting this study, as well as Marcel Guillong and Lorenzo Tavazzani for their assistance with the LA-ICP-MS analyses. We thank Donald Davis and one anonymous referee for providing constructive reviews of our manuscript and editors Klaus Mezger and Sandra Kamo for editorial handling.

**Financial support.** This research has been funded by ETH Zurich grant ETH-05 20-2.

**Review statement.** This paper was edited by Sandra Kamo and reviewed by Donald Davis and one anonymous referee.

## References

Barboni, M., Annen, C., and Schoene, B.: Evaluating the construction and evolution of upper crustal magma reservoirs with coupled U/Pb zircon geochronology and thermal modeling: A case study from the Mt. Capanne pluton (Elba, Italy), Earth Planet. Sc. Lett., 432, 436–448, https://doi.org/10.1016/j.epsl.2015.09.043, 2015.

Black, L. P. and Gulson, B. I.: The age of the Mud Tank carbonatite, Strangways Range, Northern Territory, Journal of Australian Geology and Geophysics, 3, 227–232, 1978.

Black, L. P., Kamo, S. L., Allen, C. M., Davis, D. W., Aleinikoff, J. N., Valley, J. W., Mundil, R., Campbell, I. H., Korsch, R. J., Williams, I. S., and Foudoulis, C.: Improved $^{206}Pb/^{238}U$ microprobe geochronology by the monitoring of a trace-element-related matrix effect; SHRIMP, ID-TIMS, ELA-ICP-MS and oxygen isotope documentation for a series of zircon standards, Chem. Geol., 205, 115–140, https://doi.org/10.1016/j.chemgeo.2004.01.003, 2004.

Blackburn, T. J., Olsen, P. E., Bowring, S. A., McLean, N. M., Kent, D. V., Puffer, J., McHone, G., Rasbury, E. T., and Et-Touhami, M.: Zircon U–Pb Geochronology Links the End-Triassic Extinction with the Central Atlantic Magmatic Province, Science, 340, 941–945, https://doi.org/10.1126/science.1234204, 2013.

Bowring, J. F., McLean, N. M., and Bowring, S. A.: Engineering cyber infrastructure for U–Pb geochronology: Tripoli and U–Pb_Redux, Geochem. Geophy. Geosy., 12, Q0AA19, https://doi.org/10.1029/2010gc003479, 2011.

Bowring, S. A. and Schmitz, M. D.: High-precision U–Pb zircon geochronology and the stratigraphic record, Zircon, 53, 305–326, https://doi.org/10.2113/0530305, 2003.

Bowring, S. A., Erwin, D. H., Jin, Y. G., Martin, M. W., Davidek, K., and Wang, W.: U/Pb zircon geochronology and tempo of the end-Permian mass extinction, Science, 280, 1039–1045, https://doi.org/10.1126/science.280.5366.1039, 1998.

Chelle-Michou, C., Laurent, O., Moyen, J. F., Block, S., Paquette, J. L., Couzinié, S., Gardien, V., Vanderhaeghe, O., Villaros, A., and Zeh, A.: Pre-Cadomian to late-Variscan odyssey of the eastern Massif Central, France: Formation of the West European crust in a nutshell, Gondwana Res., 46, 170–190, https://doi.org/10.1016/j.gr.2017.02.010, 2017.

Condon, D. J., Schoene, B., McLean, N. M., Bowring, S. A., and Parrish, R. R.: Metrology and traceability of U–Pb isotope dilution geochronology (EARTHTIME Tracer Calibration Part I), Geochim. Cosmochim. Ac., 164, 464–480, https://doi.org/10.1016/j.gca.2015.05.026, 2015.

Corfu, F., Hanchar, J. M., Hoskin, P. W. O., and Kinny, P.: Atlas of zircon textures, Zircon, 53, 469–500, https://doi.org/10.2113/0530469, 2003.

Costa, F., Dohmen, R., and Chakraborty, S.: Time Scales of Magmatic Processes from Modeling the Zoning Patterns of Crystals, Minerals, Inclusions and Volcanic Processes, 69, 545–594, https://doi.org/10.2138/rmg.2008.69.14, 2008.

Costa, F., Shea, T., and Ubide, T.: Diffusion chronometry and the timescales of magmatic processes, Nature Reviews Earth &

Environment, 1, 201–214, https://doi.org/10.1038/s43017-020-0038-x, 2020.

Crowley, J. L.: Laser cutting of zircon for CA-TIMS geochronology: adding spatial resolution to high-precision dates, GSA conference, Indianapolis, Indiana, USA, 4 November 2018, https://doi.org/10.1130/abs/2018AM-321517, 2018.

Curry, A., Gaynor, S. P., Davies, J. H. F. L., Ovtcharova, M., Simpson, G., and Caricchi, L.: Timescales and thermal evolution of large silicic magma reservoirs during an ignimbrite flare-up: perspectives from zircon, Contrib. Mineral. Petr., 176, 103, https://doi.org/10.1007/s00410-021-01862-w, 2021.

Davies, J. H. F. L., Marzoli, A., Bertrand, H., Youbi, N., Ernesto, M., and Schaltegger, U.: End-Triassic mass extinction started by intrusive CAMP activity, Nat. Commun., 8, 15596, https://doi.org/10.1038/ncomms15596, 2017.

Davis, W. J. and Davis, D. W.: Alpha Recoil Loss of Pb from Baddeleyite Evaluated by High-Resolution Ion Microprobe (SHRIMP II) Depth Profiling and Numerical Modeling: Implications for the Interpretation of U–Pb Ages in Small Baddeleyite Crystals, Geophys. Monogr. Ser., 232, 247–259, https://doi.org/10.1002/9781119227250, 2018.

Echlin, M. P., Straw, M., Randolph, S., Filevich, J., and Pollock, T. M.: The TriBeam system: Femtosecond laser ablation in situ SEM, Mater. Charact., 100, 1–12, https://doi.org/10.1016/j.matchar.2014.10.023, 2015.

Farina, F., Dini, A., Davies, J. H. F. L., Ovtcharova, M., Greber, N. D., Bouvier, A. S., Baumgartner, L., Ulianov, A., and Schaltegger, U.: Zircon petrochronology reveals the timescale and mechanism of anatectic magma formation, Earth Planet. Sc. Lett., 495, 213–223, https://doi.org/10.1016/j.epsl.2018.05.021, 2018.

Gain, S. E. M., Greau, Y., Henry, H., Belousova, E., Dainis, I., Griffin, W. L., and O'Reilly, S. Y.: Mud Tank Zircon: Long-Term Evaluation of a Reference Material for U–Pb Dating, Hf-Isotope Analysis and Trace Element Analysis, Geostand. Geoanal. Res., 43, 339–354, https://doi.org/10.1111/ggr.12265, 2019.

Gerstenberger, H. and Haase, G.: A highly effective emitter substance for mass spectrometric Pb isotope ratio determinations, Chem. Geol., 136, 309–312, https://doi.org/10.1016/S0009-2541(96)00033-2, 1997.

Hawkesworth, C., George, R., Turner, S., and Zellmer, G.: Time scales of magmatic processes, Earth Planet. Sc. Lett., 218, 1–16, https://doi.org/10.1016/S0012-821x(03)00634-4, 2004.

Hiess, J., Condon, D. J., McLean, N., and Noble, S. R.: $^{238}U/^{235}U$ systematics in terrestrial U-bearing minerals, Science, 335, 1610–1614, https://doi.org/10.1126/science.1215507, 2012.

Horstwood, M. S., Kosler, J., Gehrels, G., Jackson, S. E., McLean, N. M., Paton, C., Pearson, N. J., Sircombe, K., Sylvester, P., and Vermeesch, P.: Community-Derived Standards for LA-ICP-MS U-(Th-)Pb Geochronology–Uncertainty Propagation, Age Interpretation and Data Reporting, Geostand. Geoanal. Res., 40, 311–332, 2016.

Iizuka, T., Yamaguchi, A., Haba, M. K., Amelin, Y., Holden, P., Zink, S., Huyskens, M. H., and Ireland, T. R.: Timing of global crustal metamorphism on Vesta as revealed by high-precision U–Pb dating and trace element chemistry of eucrite zircon, Earth Planet. Sc. Lett., 409, 182–192, https://doi.org/10.1016/j.epsl.2014.10.055, 2015.

Ishitani, T. and Yaguchi, T.: Cross-sectional sample preparation by focused ion beam: A review of ion-sample interaction, Microsc. Res. Techniq., 35, 320–333, https://doi.org/10.1002/(SICI)1097-0029(19961101)35:4<320::AID-JEMT3>3.0.CO;2-Q, 1996.

Jackson, S. E., Pearson, N. J., Griffin, W. L., and Belousova, E. A.: The application of laser ablation-inductively coupled plasma-mass spectrometry to in situ U–Pb zircon geochronology, Chem. Geol., 211, 47–69, https://doi.org/10.1016/j.chemgeo.2004.06.017, 2004.

Jaffey, A. H., Flynn, K. F., Glendenin, L. E., Bentley, W. C., and Essling, A. M.: Precision Measurement of Half-Lives and Specific Activities of $^{235}U$ and $^{238}U$, Phys. Rev. C, 4, 1889–1906, 1971.

Jain, J. C., Neal, C. R., and Hanchar, J. M.: Problems associated with the determination of rare earth elements of a "Gem" quality zircon by inductively coupled plasma-mass spectrometry, Geostandard. Newslett., 25, 229–237, https://doi.org/10.1111/j.1751-908X.2001.tb00598.x, 2001.

Kemp, A. I. S., Vervoort, J. D., Bjorkman, K. E., and Iaccheri, L. M.: Hafnium Isotope Characteristics of Palaeoarchaean Zircon OG1/OGC from the Owens Gully Diorite, Pilbara Craton, Western Australia, Geostand. Geoanal. Res., 41, 659–673, https://doi.org/10.1111/ggr.12182, 2017.

Kennedy, A. K., Wotzlaw, J. F., Schaltegger, U., Crowley, J. L., and Schmitz, M.: Eocene Zircon Reference Material for Microanalysis of U-Th-Pb Isotopes and Trace Elements, Can. Mineral., 52, 409–421, https://doi.org/10.3749/canmin.52.3.409, 2014.

Kovacs, N., Allan, M. M., Crowley, J. L., Colpron, M., Hart, C. J. R., Zagorevski, A., and Creaser, R. A.: Carmacks Copper Cu-Au-Ag Deposit: Mineralization and Postore Migmatization of a Stikine Arc Porphyry Copper System in Yukon, Canada, Econ. Geol., 115, 1413–1442, https://doi.org/10.5382/econgeo.4756, 2020.

Krogh, T. E.: A low-contamination method for hydrothermal decomposition of zircon and extraction of U and Pb for isotopic age determinations, Geochim. Cosmochim. Ac., 37, 485–494, 1973.

Laurent, O., Björnsen, J., Wotzlaw, J. F., Bretscher, S., Silva, M. P., Moyen, J. F., Ulmer, P., and Bachmann, O.: Earth's earliest granitoids are crystal-rich magma reservoirs tapped by silicic eruptions, Nat. Geosci., 13, 163–169, https://doi.org/10.1038/s41561-019-0520-6, 2020.

McKanna, A. J., Schoene, B., and Szymanowski, D.: Geochronological and geochemical effects of zircon chemical abrasion: insights from single-crystal stepwise dissolution experiments, Geochronology, 6, 1–20, https://doi.org/10.5194/gchron-6-1-2024, 2024.

McLean, N. M., Bowring, J. F., and Bowring, S. A.: An algorithm for U–Pb isotope dilution data reduction and uncertainty propagation, Geochem. Geophy. Geosy., 12, Q0AA18, https://doi.org/10.1029/2010gc003478, 2011.

McLean, N. M., Condon, D. J., Schoene, B., and Bowring, S. A.: Evaluating uncertainties in the calibration of isotopic reference materials and multi-element isotopic tracers (EARTHTIME Tracer Calibration Part II), Geochim. Cosmochim. Ac., 164, 481–501, https://doi.org/10.1016/j.gca.2015.02.040, 2015.

Nasdala, L., Wenzel, M., Vavra, G., Irmer, G., Wenzel, T., and Kober, B.: Metamictisation of natural zircon: accumulation versus thermal annealing of radioactivity-induced damage, Contrib. Mineral. Petr., 141, 125–144, https://doi.org/10.1007/s004100000235, 2001.

Nasdala, L., Corfu, F., Schoene, B., Tapster, S. R., Wall, C. J., Schmitz, M. D., Ovtcharova, M., Schaltegger, U., Kennedy, A. K., Kronz, A., Reiners, P. W., Yang, Y. H., Wu, F. Y., Gain, S. E. M., Griffin, W. L., Szymanowski, D., Chanmuang, N. C., Ende, M., Valley, J. W., Spicuzza, M. J., Wanthanachaisaeng, B., and Giester, G.: GZ7 and GZ8-Two Zircon Reference Materials for SIMS U–Pb Geochronology, Geostand. Geoanal. Res., 42, 431–457, https://doi.org/10.1111/ggr.12239, 2018.

Paton, C., Hellstrom, J., Paul, B., Woodhead, J., and Hergt, J.: Iolite: Freeware for the visualisation and processing of mass spectrometric data, J. Anal. Atom. Spectrom., 26, 2508–2518, https://doi.org/10.1039/c1ja10172b, 2011.

Rioux, M., Garber, J. M., Searle, M., Crowley, J. L., Stevens, S., Schmitz, M., Kylander-Clark, A., Leal, K., Ambrose, T., and Smye, A. J.: The temporal evolution of subduction initiation in the Samail ophiolite: High-precision U–Pb zircon petrochronology of the metamorphic sole, J. Metamorph. Geol., 41, 817–847, https://doi.org/10.1111/jmg.12719, 2023.

Romer, R. L.: Alpha-recoil in U–Pb geochronology: effective sample size matters, Contrib. Mineral. Petr., 145, 481–491, https://doi.org/10.1007/s00410-003-0463-0, 2003.

Samperton, K. M., Schoene, B., Cottle, J. M., Keller, C. B., Crowley, J. L., and Schmitz, M. D.: Magma emplacement, differentiation and cooling in the middle crust: Integrated zircon geochronological-geochemical constraints from the Bergell Intrusion, Central Alps, Chem. Geol., 417, 322–340, https://doi.org/10.1016/j.chemgeo.2015.10.024, 2015.

Schaltegger, U., Guex, J., Bartolini, A., Schoene, B., and Ovtcharova, M.: Precise U–Pb age constraints for end-Triassic mass extinction, its correlation to volcanism and Hettangian post-extinction recovery, Earth Planet. Sc. Lett., 267, 266–275, https://doi.org/10.1016/j.epsl.2007.11.031, 2008.

Schaltegger, U., Schmitt, A. K., and Horstwood, M. S. A.: U-Th-Pb zircon geochronology by ID-TIMS, SIMS, and laser ablation ICP-MS: Recipes, interpretations, and opportunities, Chem. Geol., 402, 89–110, https://doi.org/10.1016/j.chemgeo.2015.02.028, 2015a.

Schaltegger, U., Ulianov, A., Müntener, O., Ovtcharova, M., Peytcheva, I., Vonlanthen, P., Vennemann, T., Antognini, M., and Girlanda, F.: Megacrystic zircon with planar fractures in miaskite-type nepheline pegmatites formed at high pressures in the lower crust (Ivrea Zone, southern Alps, Switzerland), Am. Mineral., 100, 83–94, https://doi.org/10.2138/am-2015-4773, 2015b.

Schoene, B.: U–Th–Pb Geochronology, Treatise on Geochemistry, 4, 341–378, 2014.

Schoene, B. and Baxter, E. F.: Petrochronology and TIMS, Rev. Mineral. Geochem., 83, 231–260, https://doi.org/10.2138/rmg.2017.83.8, 2017.

Schoene, B., Samperton, K. M., Eddy, M. P., Keller, G., Adatte, T., Bowring, S. A., Khadri, S. F. R., and Gertsch, B.: U–Pb geochronology of the Deccan Traps and relation to the end-Cretaceous mass extinction, Science, 347, 182–184, https://doi.org/10.1126/science.aaa0118, 2015.

Schoene, B., Eddy, M. P., Samperton, K. M., Keller, C. B., Keller, G., Adatte, T., and Khadri, S. F. R.: U–Pb constraints on pulsed eruption of the Deccan Traps across the end-Cretaceous mass extinction, Science, 363, 862–866, https://doi.org/10.1126/science.aau2422, 2019.

Sergeev, S. A. and Steiger, R. H.: The microtome: an innovative tool prerequisite for applying multiple high-precision/resolution analytical techniques to wafers of same sub-grain scale sample, Mineral. Mag., 63, 1365–1366, 1998.

Sergeev, S. A., Komarov, A. N., Bickel, R. A., and Steiger, R. H.: A new microtome for cutting hard submillimeter-sized crystalline objects for promoting high-resolution instrumental microanalysis, Eur. J. Mineral., 9, 449–456, 1997.

Slama, J., Kosler, J., Condon, D. J., Crowley, J. L., Gerdes, A., Hanchar, J. M., Horstwood, M. S. A., Morris, G. A., Nasdala, L., Norberg, N., Schaltegger, U., Schoene, B., Tubrett, M. N., and Whitehouse, M. J.: Plesovice zircon - A new natural reference material for U–Pb and Hf isotopic microanalysis, Chem. Geol., 249, 1–35, https://doi.org/10.1016/j.chemgeo.2007.11.005, 2008.

Smith, N. S., Notte, J. A., and Steele, A. V.: Advances in source technology for focused ion beam instruments, Mrs. Bull., 39, 329–335, https://doi.org/10.1557/mrs.2014.53, 2014.

Stern, R. A., Bodorkos, S., Kamo, S. L., Hickman, A. H., and Corfu, F.: Measurement of SIMS Instrumental Mass Fractionation of Pb Isotopes During Zircon Dating, Geostand. Geoanal. Res., 33, 145–168, https://doi.org/10.1111/j.1751-908X.2009.00023.x, 2009.

Szymanowski, D., Wotzlaw, J. F., Ellis, B. S., Bachmann, O., Guillong, M., and von Quadt, A.: Protracted near-solidus storage and pre-eruptive rejuvenation of large magma reservoirs, Nat. Geosci., 10, 777–782, https://doi.org/10.1038/Ngeo3020, 2017.

Szymanowski, D., Forni, F., Phua, M., Jicha, B., Lee, D. W. J., Hsu, Y. J., Rifai, H., Schoene, B., and Bouvet de Maisonneuve, C.: A shifty Toba magma reservoir: Improved eruption chronology and petrochronological evidence for lateral growth of a giant magma body, Earth Planet. Sc. Lett., 622, 118408, https://doi.org/10.1016/j.epsl.2023.118408, 2023.

Tavazzani, L., Wotzlaw, J. F., Economos, R., Sinigoi, S., Demarchi, G., Szymanowski, D., Laurent, O., Bachmann, O., and Chelle-Michou, C.: High-precision zircon age spectra record the dynamics and evolution of large open-system silicic magma reservoirs, Earth Planet. Sc. Lett., 623, 118432, https://doi.org/10.1016/j.epsl.2023.118432, 2023.

von Quadt, A., Wotzlaw, J.-F., Buret, Y., Large, S. J. E., Peytcheva, I., and Trinquier, A.: High-precision zircon U/Pb geochronology by ID-TIMS using new $10^{13}$ ohm resistors, J. Anal. Atom. Spectrom., 31, 658–665, https://doi.org/10.1039/c5ja00457h, 2016.

White, L. F., Tait, K. T., Kamo, S. L., Moser, D. E., and Darling, J. R.: Highly accurate dating of micrometre-scale baddeleyite domains through combined focused ion beam extraction and U–Pb thermal ionization mass spectrometry (FIB-TIMS), Geochronology, 2, 177–186, https://doi.org/10.5194/gchron-2-177-2020, 2020.

White, N., Eder, K., Byrnes, J., Cairney, J. M., and McCarroll, I. E.: Laser ablation sample preparation for atom probe tomography and transmission electron microscopy, Ultramicroscopy, 220, 113161, https://doi.org/10.1016/j.ultramic.2020.113161, 2021.

Wiedenbeck, M., Alle, P., Corfu, F., Griffin, W. L., Meier, M., Oberli, F., von Quadt, A., Roddick, J. C., and Spiegel, W.: Three natural zircon standards for U-Th-Pb, Lu-Hf, trace element and REE analyses, Geostandard. Newslett., 19, 1–23, https://doi.org/10.1111/j.1751-908X.1995.tb00147.x, 1995.

Wiedenbeck, M., Hanchar, J. M., Peck, W. H., Sylvester, P., Valley, J., Whitehouse, M., Kronz, A., Morishita, Y., Nasdala, L., Fiebig, J., Franchi, I., Girard, J. P., Greenwood, R. C., Hinton, R., Kita, N., Mason, P. R. D., Norman, M., Ogasawara, M., Piccoli, R., Rhede, D., Satoh, H., Schulz-Dobrick, B., Skar, O., Spicuzza, M. J., Terada, K., Tindle, A., Togashi, S., Vennemann, T., Xie, Q., and Zheng, Y. F.: Further characterisation of the 91500 zircon crystal, Geostand. Geoanal. Res., 28, 9–39, https://doi.org/10.1111/j.1751-908X.2004.tb01041.x, 2004.

Woodhead, J. D. and Hergt, J. M.: A preliminary appraisal of seven natural zircon reference materials for Hf isotope determination, Geostand. Geoanal. Res., 29, 183–195, https://doi.org/10.1111/j.1751-908X.2005.tb00891.x, 2005.

Wotzlaw, J. F., Bindeman, I. N., Schaltegger, U., Brooks, C. K., and Naslund, H. R.: High-resolution insights into episodes of crystallization, hydrothermal alteration and remelting in the Skaergaard intrusive complex, Earth Planet. Sc. Lett., 355, 199–212, https://doi.org/10.1016/j.epsl.2012.08.043, 2012.

Wotzlaw, J. F., Bindeman, I. N., Stern, R. A., D'Abzac, F. X., and Schaltegger, U.: Rapid heterogeneous assembly of multiple magma reservoirs prior to Yellowstone supereruptions, Sci. Rep.-UK, 5, 14026, https://doi.org/10.1038/srep14026, 2015.

Wotzlaw, J. F., Buret, Y., Large, S. J. E., Szymanowski, D., and von Quadt, A.: ID-TIMS U–Pb geochronology at the 0.1 ‰ level using $10^{13}\Omega$ resistors and simultaneous U and $^{18}O/^{16}O$ isotope ratio determination for accurate $UO_2$ interference correction, J. Anal. Atom. Spectrom., 32, 579–586, https://doi.org/10.1039/c6ja00278a, 2017.